Cassini Encounters Enceladus: Background, and Discovery of a South Polar Hot Spot

J. R. Spencer[1*], J. C. Pearl[2], M. Segura[2], F. M. Flasar[2], A. Mamoutkine[2], P. Romani[2], B. J. Buratti[3], A. R. Hendrix[3], L. J. Spilker[3], R. M. C. Lopes[3]

[1]Dept. Space Studies, Southwest Research Institute, 1050 Walnut St, Suite 400, Boulder CO 80302

[2]NASA's Goddard Spaceflight Center, Greenbelt, MD 20771

[3]Jet Propulsion Laboratory, California Institute of Technology, 4800 Oak Grove Drive, Pasadena, CA 91109

[*]To whom correspondence should be addressed.

E-mail: spencer@boulder.swri.edu

Phone: 303 546-9674

Fax: 303 546-9687

Submitted to *Science*, Enceladus special issue, October 20th 2005

Revised Version, December 22nd 2005

Abstract

The Cassini spacecraft completed three close flybys of Saturn's enigmatic moon Enceladus betwee February and July 2005. On the third flyby and closest flyby, on July 14th 2005, multiple Cassini instruments detected evidence for ongoing endogenic activity in a region centered on Enceladus' south pole. The polar region is the source of a plume of gas and dust which probably emanates from prominent warm troughs seen on the surface. Cassini's Composite Infrared Spectrometer detected 3 – 7 GW of thermal emission from the south polar troughs at temperatures up to 145 K or higher, making Enceladus only the third known solid planetary body, after the Earth and Io, that is sufficiently geologically active that its internal heat can detected by remote sensing. If the plume is generated by sublimation of H_2O ice, and the sublimation source is visible to CIRS, sublimation temperatures of at least 180 K are required.

Introduction

Cassini-Huygens is a major international planetary mission that entered orbit around Saturn on July 1, 2004 for a nominal 4-year investigation of the planet, its satellites, rings, and magnetosphere. In 2005 Cassini made three flybys of the enigmatic satellite Enceladus, long suspected to be recently geologically active and the source of Saturn's tenuous, extended E-ring. Results from multiple Cassini instruments on the third flyby, on July 14th 2005, offer convincing proof that this small icy satellite is currently active, as described in the following series of companion papers.

Enceladus

Discovered by William Herschel in 1789, Enceladus orbits close to Saturn at radius of 4.0 Saturn radii, and thus is difficult to observe from Earth due to the scattered light of the

planet and its rings. Its orbital period is 1.37 days. Telescopic infrared spectra indicate a surface composed of almost pure water ice (*0*) though a tentative detection of ammonia ice has been reported recently (*0*). The Voyager encounters with the satellite in 1981 established its radius (249 km) (*3*), and that its visual geometric albedo is startlingly high, consistent with fresh snow or ice and higher than for any other known solar system body (*4*,*5*). Voyager 2 also discovered that Enceladus was unique among Saturn's medium-sized icy satellites because its surface includes sizable crater-free areas that have been resurfaced by endogenic forces (*4*) and were estimated to be <200 my in age (*6*). Other parts of the satellite are heavily cratered and perhaps nearly as old as the solar system, but the craters show considerable signs of internal modification. All regions of the satellite, regardless of age, exhibit uniformly high albedos, implying that the entire satellite is coated with a ubiquitous fresh material (*7*). Particle orbit models have shown that Enceladus is probably the major source of the tenuous E-ring (*8*), which is most dense at the satellite's orbit. The mechanism for the injection of material from the satellite into the E-ring has been debated: volcanism (*9*), geysers (*10*), large impacts (*11*), and collisions between Enceladus and E-ring particles themselves (*12*) have all been proposed. Regardless of the means of transport, the micron-sized particles that comprise the ring must be constantly replenished, as sputtering (*10*,*13*) would destroy them on time scales much shorter than the age of the solar system.

The heat source for the extensive resurfacing on an object as small as Enceladus has always been difficult to explain, especially when compared to other Saturnian satellites that show much less evidence of activity (*14*,*15*,*16*). The orbital eccentricity of Enceladus, (0.0045, comparable to that of Io) is perhaps sufficient for significant tidal

heating given the right internal structure (*16*), but the absence of internal activity on nearby Mimas, which has an orbital eccentricity of 0.020, makes this source problematic too. The contrast with Mimas might be explained if Mimas is in a cold, elastic, non-dissipative state while Enceladus is in a self-maintaining warm, plastic, dissipative state (*17*). Resonantly-excited rotational librations have recently been suggested as a possible alternative tidal heating mechanism (*18*,*19*).

Cassini Flybys

Cassini has observed Enceladus with multiple instruments including the Ultraviolet Imaging Spectrometer (UVIS), the visible-wavelength Imaging Science Subsystem (ISS), the Visible and Near Infrared Mapping Spectrometer (VIMS), the Composite Infrared Spectrometer (CIRS), the magnetometer (MAG), the Cosmic Dust Analyzer (CDA), the Cassini Plasma Spectrometer (CAPS), the Radio and Plasma Wave Science (RPWS) instrument, and the Ion and Neutral Mass Spectrometer (INMS). The first close Cassini flyby of Enceladus, on orbit 3 on February 17th 2005, at an altitude of 1263 km (Table 1), focused on the equatorial region centered near longitude 310 W. ISS revealed a world scarred by extensive tectonic activity (*19*), and VIMS spectra indicated that the surface composition was completely dominated by water ice (*20*). MAG data showed a draping of Saturn's magnetic field lines around the moon, which suggested the presence of an atmosphere (*21*). However, UVIS observations of a stellar occultation observed by UVIS showed no sign of an atmosphere at low latitudes (*22*). During the second flyby, on orbit 4 at 501 km altitude on March 9th 2005, Cassini concentrated on the equatorial region of the hemisphere centered near 190 W. ISS images revealed complex networks of ridges and troughs coexisting with ancient cratered plains. MAG measured a signature in

addition to the one seen in February, possibly indicating an induced or intrinsic magnetic field. Based on the MAG results the Cassini Project decided to reduce the altitude of the July 14th 2005 encounter, on orbit 11, from 1000 km down to 175 km.

On the July 14th flyby the spacecraft approached the illuminated anti-Saturn hemisphere, which centered on longitude 180 W, from the south. On approach, the remote sensing instruments (ISS, VIMS, UVIS, and CIRS) observed Enceladus beginning 8 hours prior to closest-approach, starting from a distance of 288,000 km. At 21 min before closest approach, the spacecraft began the turn to point to the star γ-Orionis (Bellatrix) and at 4 min before closest approach, Bellatrix was occulted by Enceladus; measurements of the occultation were performed by UVIS (*22*). As Enceladus passed in front of the star, the moon crossed through the boresights of the remote sensing instruments, providing a brief opportunity for remote sensing at very high spatial resolution. The sub-spacecraft point at closest approach was at 24 S 326 W. Post-occultation, at 3 min after closest approach, the spacecraft began to turn back to Enceladus and resumed remote sensing of the nighttime surface at +31 minutes, continuing to +114 minutes. Throughout the inbound and outbound portions of the flyby and during closest approach, the fields and particles instruments obtained valuable information on the plasma and particulate environment around Enceladus. In particular, INMS (*23*), CAPS and RPWS (*24*) and CDA (*25*) obtained in situ measurements of the near-south polar environment.

Composite Infrared Spectrometer Results

The CIRS instrument (*26*) used the three Enceladus encounters to investigate the satellite's thermal radiation, which provides clues to its surface properties and a means to detect possible endogenic activity. The only previous observations of Enceladus' thermal

radiation were by Voyager 2 in 1981 (*27*), which derived a disk-integrated 250 cm^{-1} brightness temperature (*28*) of 67 K at 37 degree phase angle with an inferred subsolar temperature of 75 ± 3 K, but provided little other information. CIRS consists of two Fourier transform spectrometers, which together measure thermal emission from 10 to 1400 cm^{-1} (wavelengths 1 mm to 7 μm) at a selectable spectral resolution between 0.5 and 15.5 cm^{-1}. The far infrared interferometer (10 to 600 cm^{-1}) has a 4-mrad field of view on the sky. The mid-infrared interferometer consists of two 1 × 10 arrays of 0.3 mrad pixels, which together span 600 to 1400 cm^{-1}.

Cassini's first two flybys of Enceladus, in February and March 2005, provided good views of the low-latitude regions on both sides of the satellite. Daytime thermal emission from the anti-Saturn side of the moon was mapped by the far-IR detector in March 2005 and the same region was seen at night in February 2005 (Fig. 1A). Most spectra are well described by blackbody curves in the 50 – 600 cm^{-1} range, and we estimate surface temperature by least-squares fitting of blackbody curves to the spectra. Comparison of daytime and nighttime temperatures for the same regions allows determination of bolometric albedo and thermal inertia (*29*) as a function of location on this hemisphere. Nighttime temperatures showed significant spatial variability, probably resulting from thermal inertia variations: day and night temperatures near longitude 180 W can be matched by models with thermal inertias in the range 12 – 25 J m^{-2} $s^{-1/2}$ K^{-1}, averaged over the uppermost ~1 cm of the surface layer, while bolometric albedo on this hemisphere is more constant, varying between 0.80 and 0.82 (Fig. 1B). These bolometric albedos are consistent with the estimate from Voyager photometry of 0.90 ± 0.10 (*30*), and subsolar temperatures, near 76 K, are also consistent with Voyager estimates (*27*).

The thermal inertia is 100 times smaller than that of solid water ice (*31*), implying a highly unconsolidated surface.

The third flyby, on orbit 11 on July 14th 2005, provided the first good view of the south polar regions of Enceladus. Maps of the daytime thermal emission were obtained with both the mid-IR and far-IR detectors on approach. The low spatial resolution of the far-IR detector prevented good observations of the south polar region at long wavelengths (Fig. 1A), but the mid-IR detector was able to map the entire disk at a spatial resolution of 25 km over the 600 – 800 cm^{-1} (12.5 – 16 μm) spectral range, with useful signal at higher wavenumbers in the warmest regions (Fig. 2A,B). The equatorial regions showed 650 cm^{-1} brightness temperatures in the high 70s K, consistent with models of passive solar heating based on the range of thermal inertias and albedos determined from the earlier flybys (Fig. 1). However, most of the polar region south of latitude 65 S showed higher brightness temperatures, reaching 85 K near the south pole. This temperature is surprisingly warm: the temperature at the south pole that is in equilibrium with current insolation (i.e., assuming zero thermal inertia) is only 68 K for an albedo of 0.81, because of the highly oblique illumination there (solar elevation at the pole was only 23 degrees). An implausibly low south polar albedo of 0.55, 67% of the equatorial albedo, would be necessary to increase the equilibrium temperature to 85 K. The elevated temperatures are not due to seasonal effects: we modeled long-term seasonal variations in the south polar temperature due to changes in the subsolar latitude and heliocentric distance of Enceladus, for a range of thermal inertias, and found that at the current season (midway between the southern summer solstice and the fall equinox) the south polar temperature is lower still for non-zero thermal inertia. The region of elevated south polar temperatures

corresponds closely to a geologically youthful region occupied by four prominent troughs (dubbed "tiger stripes") seen by the Cassini cameras (Fig. 2B) (*19*).

The spectrum of the south polar thermal emission yields evidence for even higher temperatures, making an origin from solar heating even less likely. We found that the south polar spectrum was not well fit by a single-temperature blackbody filling the field of view. After subtracting the expected background thermal emission from a solar-heated surface, assuming a model with an albedo of 0.81 and thermal inertia of 20 J m^{-2} $s^{-1/2}$ K^{-1}, the average spectrum of the 37,000 km^2 region south of 65 S could be fitted perfectly, within the uncertainties, by a graybody (i.e. a blackbody multiplied by a wavelength-independent filling factor) of temperature 133 ± 12 K occupying 340 $^{+320}_{-160}$ km^2 (Fig. 2C). We determined uncertainties in the fit parameters by a Monte Carlo technique. We first determined noise levels (which are dominated by instrumental noise) from the scatter of the observed spectrum around the best fit model. We then added that noise level to the model, refitted the noisy model spectrum, and repeated this process many times to determine the probability distribution of fit parameters (Figs. 2D,E). The probability distribution of fitted temperatures (Fig 2D) suggests that maximum temperatures below 110 K are highly unlikely.

The spectral fits allow estimation of the total radiated power from the south polar region. After adjusting fitted temperatures for the thermal contribution expected from sunlight absorbed by the hot regions on the assumption that the hot sources have the same albedo (~0.81) as the rest of the surface, we derive a radiated non-solar power of 5.8 ± 1.9 GW (Fig 2F). Even if the hot sources have an albedo of 0.0 (highly unlikely, but not formally ruled out, as the hot regions could be mixed with higher albedo regions on spatial scales

too small to be resolved) the non-solar power is still 3.9 GW. These estimates do not include the potential power contributions from the kinetic and latent heat of the south polar plume seen by other Cassini instruments (*21*,*22*,*23*,*24,25*), or any heat radiated at lower temperatures. For comparison, the total endogenic power radiated by Io is ~10^5 GW (*32*), and Enceladus' power generation per unit volume, assuming all the heat escapes from the south pole, is 3% that of Io. Assuming the heat is generated below the surface, the average heat flow over the region south of 65 S is 0.25 W m^{-2}, compared to ~2.5 W m^{-2} for Io (*32*). The depth to melting, or to ice warm and ductile enough to transport heat by convection, assuming pure solid H_2O ice and an ice conductivity of 3 x 10^5 erg cm^{-1} s^{-1} K^{-1} at the mean temperature of 180 K (*33*), is then only 2.5 km if the heat is generated below this level. In the hot regions at 124 K, heat flow is 13 W m^{-2} and solid H_2O ice will approach the melting temperature at a depth of only 40 m. It is perhaps more likely that the heat is transported to the surface by advection of warm vapor rather than by conduction.

The relationship to the geological features becomes clearer in higher-resolution CIRS observations obtained during the last 2.5 hours of the approach to Enceladus. In this period CIRS did not perform contiguous scans of Enceladus, but instead rode along with the pointing determined by the ISS cameras as they obtained imaging mosaics of the moon, resulting in very scattered coverage with mid-IR spatial resolution as fine as 50 m near closest approach (Fig 3A). These higher resolution observations confirm that the thermal emission is highly localized and is associated with individual prominent "tiger stripe" troughs (*19*). The spatial correlation is not perfect, but discrepancies can perhaps be ascribed to pointing uncertainties. In some cases the pointing uncertainties can be

eliminated because CIRS observations were obtained near-simultaneously with camera exposures, and the ISS field of view includes the 1 x 10 pixel CIRS mid-IR field of view. The location of the thermal emission observations relative to the geological features can then be determined very precisely (Fig 3B,C), confirming the association with the troughs, though there also seems to be some thermal emission from regions adjacent to the troughs. Table 2 describes the seven discrete hot sources that can be identified with greatest confidence in the ride-along observations, either because of simultaneous imaging or particularly strong thermal emission (Fig 3A). We fitted blackbodies to the spectra of these sources after subtracting spectra of adjacent regions taken with the same CIRS detector, thus removing, to first order, the small contribution of thermal emission from the background and reducing calibration uncertainties. The association of the hot sources with linear features makes it likely that the hot sources are themselves linear, and Table 2 lists the inferred width of each source on the assumption that it is a linear feature extending across and beyond the CIRS field of view. The hot regions appear to be typically hundreds of meters wide. The some of the hottest individual spectra (sources C - G) were obtained during slews between ISS mosaic positions, and thus cannot be located so precisely, though they also appear to be close to the "tiger stripe" troughs. The brightest spectrum, D, requires a temperature of 145 ± 14 K, with temperatures below 120 K being highly unlikely (Fig. 3D,E,F).

CIRS observed the north pole of Enceladus after closest approach, and though mid-IR coverage is more limited than at the south pole, we can rule out a similar hot spot in the north. A far-IR integration of a 80 km diameter region centered on the north pole, which has been in darkness since 1995, determined a best-fit temperature of 32.9 ± 1.2 K (Fig.

1C), though to be conservative, this should be considered an upper limit because of the possibility that scattered radiation from surrounding warmer regions contaminated the signal. The corresponding thermal inertia, averaged over the penetration depth of the seasonal thermal wave (about 1 meter), is < 100 J m^{-2} $s^{-1/2}$ K^{-1}. Any north polar hot component at the temperature of the south polar spot (133 K) would have to have less than 15% of the heat flow of the south polar spot in order to avoid detection in this integration. The lack of a north polar hot spot is consistent with the presence of heavily cratered terrain at the north pole (*4*,*6*).

Discussion

It is likely that these warm troughs are the source of the dust and vapor plume seen by other Cassini instruments (*21*,*22*,*23*,*24,25*). From a stellar occultation measurement, UVIS detected a vapor plume above the south polar region (*22*), and determined an escape rate of 5 – 10 x 10^{27} molecules/sec. If we assume that the immediate origin of this plume is thermal sublimation of warm water ice (or the plume is in vapor pressure equilibrium with surface ice at its source), and that this warm ice is visible to the CIRS instrument (rather than being hidden in deep fractures, for instance), we can constrain the temperature of the plume source using the observed thermal emission from the south pole. The mean south polar radiance radiance at 900 cm^{-1}, about 5 x 10^{-10} W cm^{-2} str^{-1} $(cm^{-1})^{-1}$ (Fig. 2C), places an upper limit on the exposed area of a high-temperature plume source at a given temperature, and thus, using the vapor pressure curve for water ice (*34*), an upper limit to the sublimation rate from this source. The UVIS escape rate can be reconciled with the observed 900 cm^{-1} radiance only for plume source temperatures of 180 K or higher. A 180 K plume source would have an area of 28 km^2, equivalent for

instance to a 50 meter width along each of the four ~130 km long tiger stripes (*19*), to produce the UVIS lower limit H_2O flux. 180 K is close to the 173 K temperature of a water/ammonia eutectic melt, a plausible cryovolcanic fluid within Enceladus (*14*), but the correspondence may be coincidental as ammonia was not detected in the plume by the INMS instrument (*23*).

The presence of these high temperatures at the south pole of Enceladus is surprising. As described above, the temperatures in many places are too high to be due to simple re-radiation of sunlight absorbed at the surface. Very high subsurface temperatures can in theory be produced by subsurface trapping of solar radiation, the so-called solid-state greenhouse effect (*35*), and might generate warm gases that could escape along fractures and form plumes, as has been proposed for Neptune's moon Triton (*36*). However, sufficiently large temperature enhancements have not been demonstrated in practice, and the association of the heat with obviously endogenic geological features (*19*) also makes a solar heating origin unlikely. An endogenic heat source is thus the most plausible explanation for the high temperatures. Maximum available power from radiogenic heat, assuming a chondritic composition for the non-ice material in Enceladus, is about 0.1 GW (*15*), much smaller than observed, but tidal heating might generate 10 -100 x more heat (*37*), comparable to the observed value. It is also possible that Enceladus is in an oscillatory state, as has been proposed for Io and Europa (*38*). In that case, its eccentricity and tidal heating rate may have recently been much higher, and perhaps the moon is still cooling down from that period.

In summary, the Cassini CIRS instrument has found that Enceladus is radiating at least several GW of endogenic heat at temperatures of up to 145 K or higher. Comparison

with ISS images (*39*) shows that the heat is concentrated along surface troughs. These warm troughs are presumably the source of the vapor and dust plumes seen by other Cassini instruments.

Tables

Table 1: Cassini Enceladus encounter geometries

Cassini Orbit	Date	Time	Altitude at closest approach (km)	Approach Geometry, 2 hours before encounter	
				Subspacecraft lat, long.	Phase angle
3	February 17, 2005	03:30	1263	309 W, 0 N	25
4	March 9, 2005	09:08	501	191 W, 1 S	47
11	July 14, 2005	19:55	173	186 W, 47 S	47

Table 2: Selected discrete hot sources identified by CIRS

Hot Source Designation	Latitude	Longitude	CIRS Resolution (km)	Best-Fit Graybody		
				Temperature	Filling Factor	Width if Linear
A	69 S	171 W	17.5	114 ± 22	0.063	1100 m
B	84 S	137 W	6.0	117 ± 16	0.092	550 m
C	87 S*	236 W*	5.8	135 ± 9	0.082	480 m
D	80 S*	289 W*	5.8	145 ± 14	0.046	250 m
E	78 S*	78 W*	13.6	133 ± 28	0.035	480 m
F	75 S*	328 W*	13.3	157 ± 24	0.017	230 m
G	76 S*	115 W*	6.0	127 ± 28	0.053	320 m

*Approximate location: no simultaneous imaging

References and Notes

1. D. P. Cruikshank, *Icarus* **41**, 246 (1980).

2. J. P. Emery, D. M. Burr, D. P. Cruikshank, R. H. Brown, J. B. Dalton, *Astron. Astrophys.* **435**, 353 (2005).

3. S. F. Dermott, P. C. Thomas, *Icarus* **109**, 241 (1994).

4. B. A. Smith *et al.*, *Science* **215**, 505 (1982).

5. A. J. Verbiscer, R. G. French, C. A. McGhee, *Icarus* **173**, 66 (2005).

6. J. S. Kargel, S. Pozio, *Icarus* **119**, 385 (1996).

7. B. J. Buratti, *Icarus* **75**, 113 (1988).

8. M. Horanyi, J. A. Burns, D. P. Hamilton, *Icarus* **97**, 248 (1992).

9. K. D. Pang, C. C. Voge, J. W. Rhoads, J. M. Ajello, *J. Geophys. Res.* **89**, 9459 (1984).

10. P. K. Haff, G. L. Siscoe, A. Eviatar, *Icarus* **56**, 426 (1983).

11. W. B. McKinnon, *Lunar Planet. Sci. Conf.* **14**, 487 (1983).

12. D. P. Hamilton, J. A. Burns, *Science* **264**, 550 (1994).

13. S. Jurak, R. E. Johnson, J. D. Richardson, *Icarus* **149**, 384 (2001).

14. S. W. Squyres, R. T. Reynolds, P. M. Cassen, *Icarus* **53**, 319 (1983).

15. G. Schubert, T. Spohn, R. T. Reynolds, in *Satellites*, J. Burns, M. Matthews, Eds. (U. Arizona Press, Tucson, AZ), pp. 224-292 (1986).

16. M. N. Ross, G. Schubert, *Icarus* **78**, 90 (1989).

17. L. Czechowski, J. Leliwa-Kopystyński, *Planet. Space Sci.* **53**, 749 (2005).

18. J. Wisdom, *Astron. J.* **128**, 484 (2004).

19. C. Porco et al., this volume

20. R. H. Brown et al., this volume.

21. M. K. Dougherty et al. this volume.

22. C. J. Hansen et al., this volume.

23. H. Waite et al., this volume

24. R. L. Tokar et al., this volume.

25. F. Spahn et al., this volume

26. M. Flasar *et al.*, *Space Sci. Rev.* **115**, 169 (2004).

27. R. Hanel *et al*., *Science* **215**, 544 (1982).

28. Brightness temperature is the temperature of a blackbody emitting the observed flux at the observed wavelength

29. Thermal inertia, defined as $\sqrt{(k\rho c)}$, where k is the thermal conductivity, ρ is the density, and c is the specific heat, describes the ability of a surface to resist temperature changes caused by changes in insolation.

30. B. Buratti, J. Veverka, *Icarus* **58**, 254 (1984).

31. J. R. Spencer *et al.*, in *Pluto and Charon*, S. A. Stern, D. Tholen, Eds. (U. Arizona Press, Tucson, AZ), pp 435-473 (1997).

32. A.S. McEwen, L. P. Keszthelyi, R. Lopes, P. M. Schenk, J. R. Spencer, in *Jupiter, the Planet, Satellites, and Magnetosphere*, F. Bagenal, T. Dowling, W. McKinnon, Eds. (U. Cambridge Press, Cambridge, UK), pp 307-328 (2004).

33. J. Klinger, 1980, *Science* **209**, 271 (1980).

34. C. E. Bryson, V. Cazcarra, L. L. Levenson, *J. Chem. Eng. Dat.* **19**, 107-110 (1974).

35. D. L. Matson, R. H. Brown, *Icarus* **77**, 61 (1989).

36. R. H. Brown, R. L. Kirk, T. V. Johnson, L. A. Soderblom, *Science* **250**, 431 (1990).

37. L. Czechowski, paper presented at the 35th COSPAR Scientific Assembly, Paris, France, 18 July 2004.

38. H. Hussmann, T. Spohn, *Icarus* **171**, 391 (2004).

39. CIRS and ISS are acknowledged in the co-discovery of the correlation between the hot spots and the tiger stripe fractures.

40. We acknowledge the invaluable support of the entire Cassini science and engineering teams in making these observations possible. The work was supported by the NASA Cassini Project.

Figure Captions

Figure 1 Far-IR observations of Enceladus. (**A**) Far-IR brightness temperature images of the nighttime and daytime thermal emission from the anti-Saturn hemisphere of Enceladus (centered at longitude 180 W), from the three Cassini encounters. Apparent signal beyond the limb of Enceladus is an artifact of the low spatial resolution and the plotting technique. (**B**) Thermal model fits to the far-IR day and night brightness temperatures at longitude 180 W and two different latitudes, as measured on orbits 3 and 4, showing the large spatial variations in thermal inertia (T.I., in MKS units). (**C**) Far-IR spectrum of the north pole, with best-fit blackbody and graybody spectra, showing the lack of the high-temperature component seen at the south pole. The fine structure in this and all spectra shown is due to noise.

Figure 2 (**A**) Mid-infrared brightness temperature image of Enceladus from Rev. 11, showing the prominent south polar hot spot. The dashed line is the terminator. (**B**) Brightness temperature contours derived from the observation in **A**, superposed on an ISS basemap (*19*), showing the spatial correlation of the hot material with the region containing the "tiger stripe" troughs. Spatial resolution of the temperature map is about 50 km after projection and smoothing. The yellow dashed line shows the latitude boundary of the average spectrum shown in **C**. (**C**) Thermal emission spectrum of the region south of latitude 65 S, compared to the best-fit blackbody spectrum, which does not match the data, and the best-fit graybody + background model spectrum, which matches the data very well. (**D**), (**E**), and (**F**). Probability distributions for the temperature, filling factor, and total radiated power for the hot material in the south polar region, on the assumption of a single temperature for the

hot material, derived by Monte Carlo techniques. The power distribution is shown for assumed albedos of 0.81 and 0.00.

Figure 3 (**A**) Color-coded south polar brightness temperatures at high spatial resolution, derived from the ISS ride-along CIRS observations, superposed on an ISS basemap (*19*), showing the correlation between high brightness temperatures and the individual "tiger stripe" troughs. Isolated colored rectangles represent observations taken during slews, and have less reliable locations than other observations. The locations of the four hot sources described in Table 1 and the rest of this figure are indicated. (**B**) and (**C**) Precise location of hot sources A and B relative to the topography as derived from simultaneous ISS images (*19*). Each box shows a single mid-infrared field of view and its associated brightness temperature, with uncertainties: field of view size is 17.5 km for source A and 6.0 km for source B. (**D**) The hottest individual CIRS spectrum (source D), and the best fit graybody spectrum. (**E**) and (**F**) Probability distribution of the temperature and filling factor for the spectrum of source D, on the assumption of a single temperature.

A. Far-IR Images

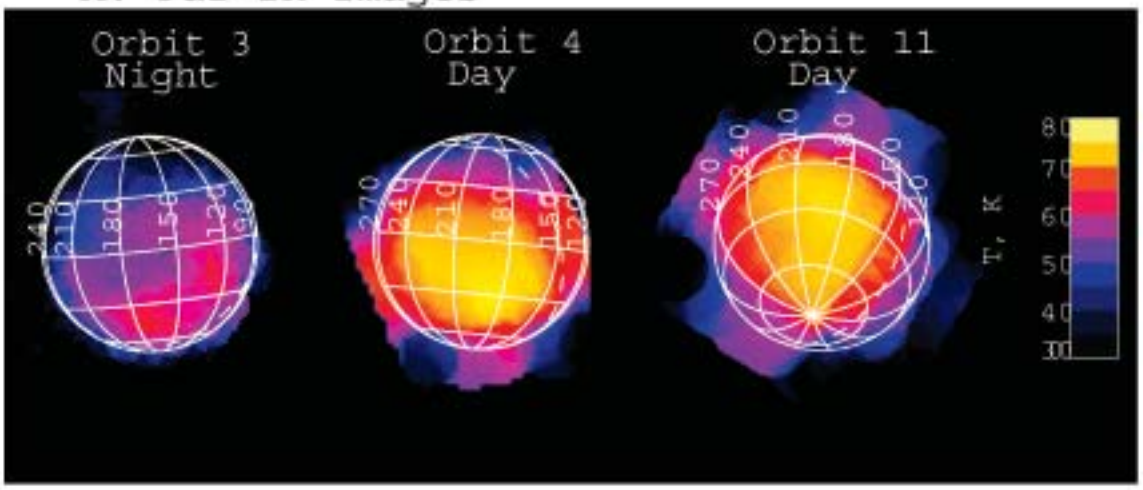

B. Diurnal Temperatures

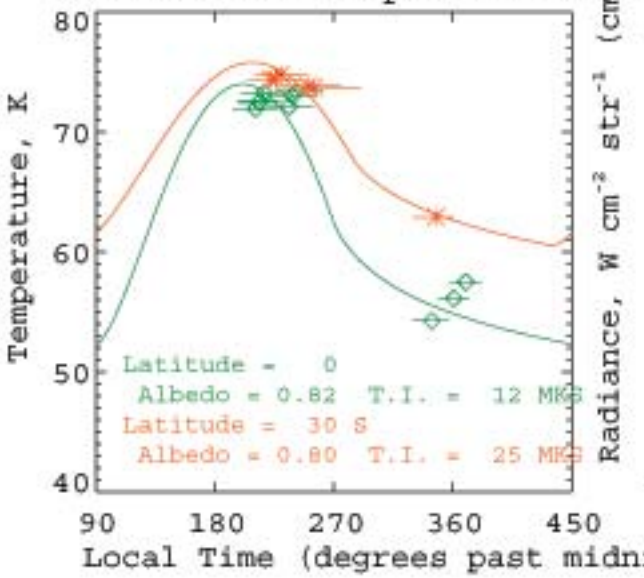

180 W. North Polar Spectrum

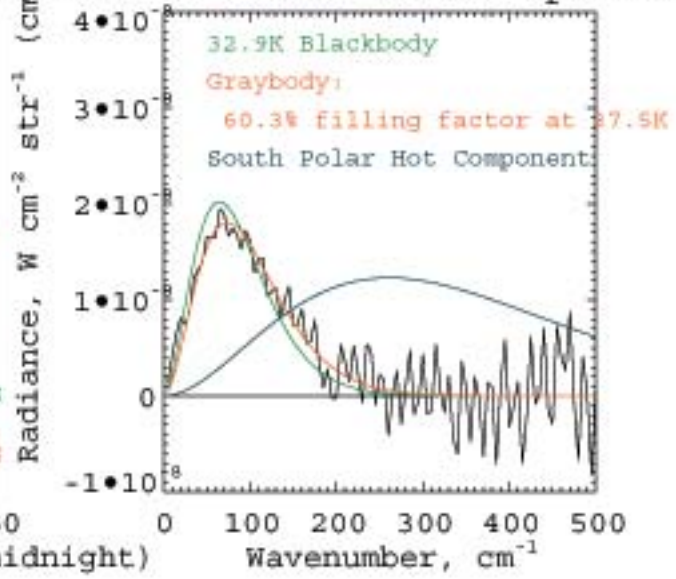

A. 600 - 800 cm^{-1} Image

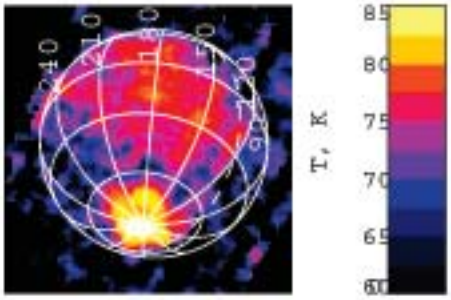

C. South Polar Spectrum

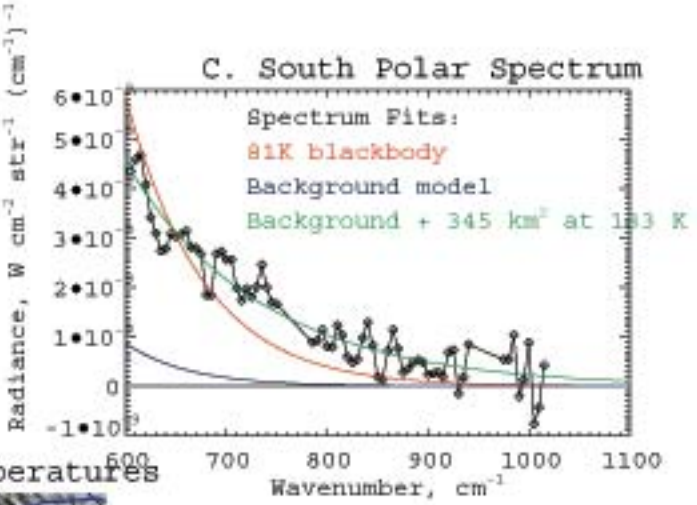

B. South Pole Brightness Temperatures

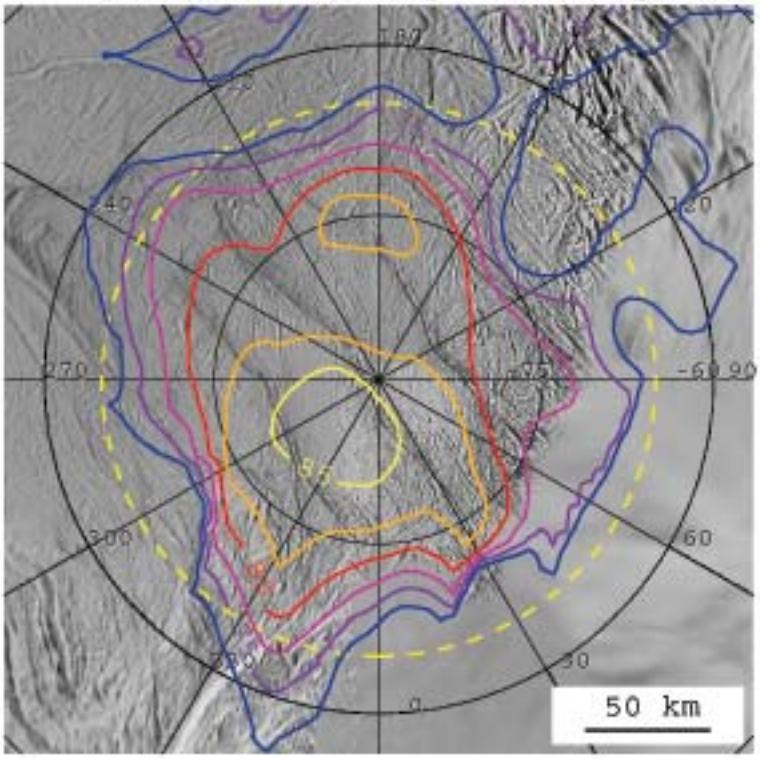

D. Temperature Uncertainty

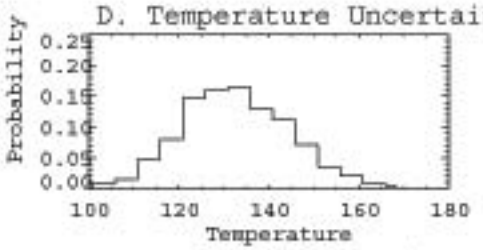

E. Area Uncertainty

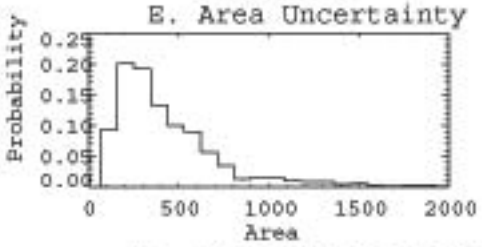

F. Power Uncertainty

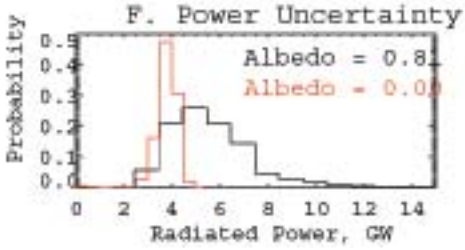

A. South Pole Hi-Res Brightness Temperatures

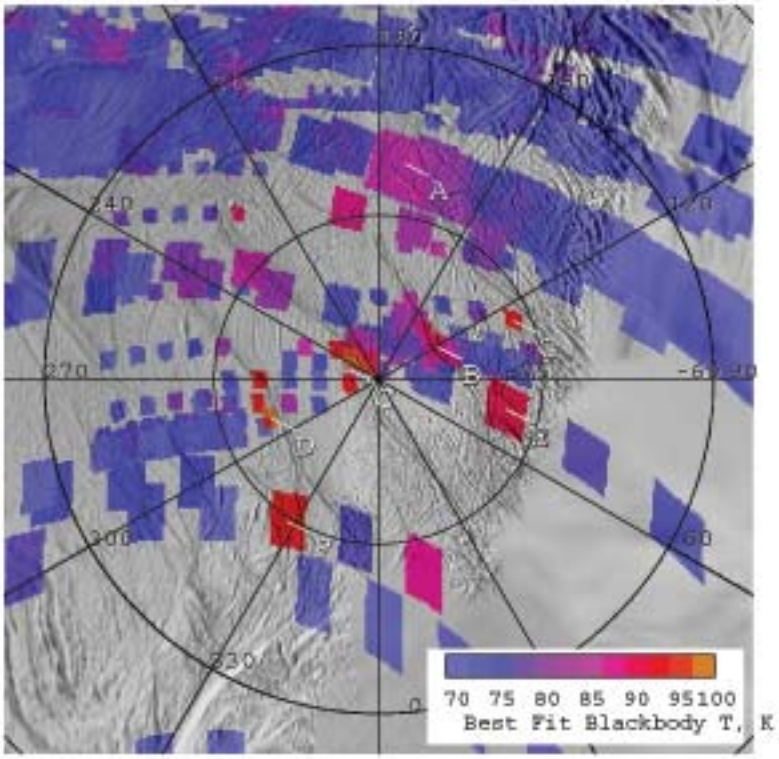

B. Hot Source A Location

C. Hot Source B Location

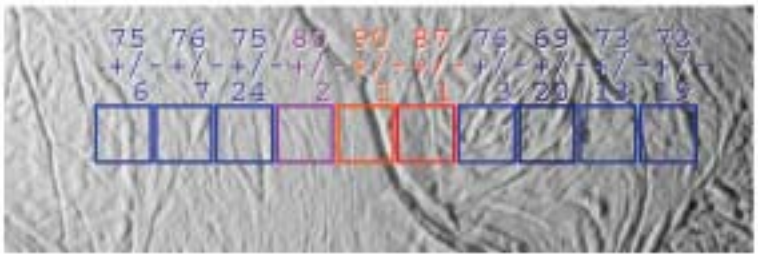

D. Hot Source D Spect

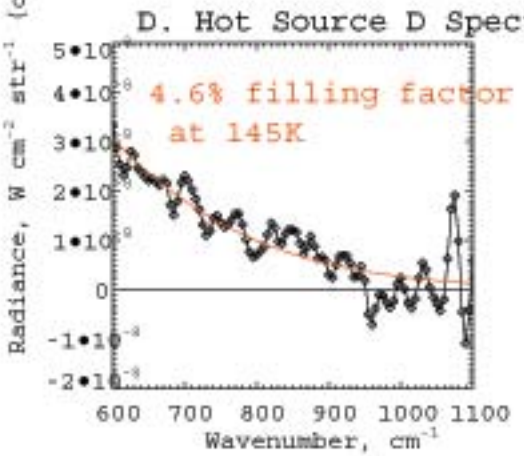

E. Temperature Uncerta

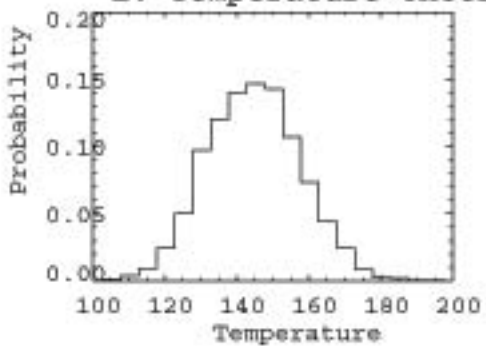

F. Filling Factor Unce